

Accepted Manuscript

Design of high speed InGaAs/InP one-sided junction photodiodes with low junction capacitance

Jie Xu, Xiupu Zhang, Ahmed Kishk

PII: S0030-4018(18)31142-8

DOI: <https://doi.org/10.1016/j.optcom.2018.12.085>

Reference: OPTICS 23753

To appear in: *Optics Communications*

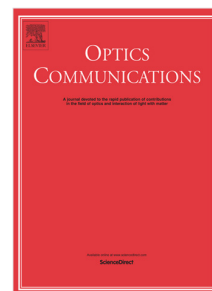
Received date: 26 February 2018

Revised date: 15 December 2018

Accepted date: 27 December 2018

Please cite this article as: J. Xu, X. Zhang and A. Kishk, Design of high speed InGaAs/InP one-sided junction photodiodes with low junction capacitance, *Optics Communications* (2018), <https://doi.org/10.1016/j.optcom.2018.12.085>

This is a PDF file of an unedited manuscript that has been accepted for publication. As a service to our customers we are providing this early version of the manuscript. The manuscript will undergo copyediting, typesetting, and review of the resulting proof before it is published in its final form. Please note that during the production process errors may be discovered which could affect the content, and all legal disclaimers that apply to the journal pertain.



Design of High Speed InGaAs/InP One-Sided Junction Photodiodes with Low Junction Capacitance

Jie Xu ^a, Xiupu Zhang ^{a,*}, Ahmed Kishk ^b

^a *Photonics Laboratories, Department of Electrical and Computer Engineering, Concordia University, Montreal, Quebec, H3G 1M8, CANADA*

^b *Department of Electrical and Computer Engineering, Concordia University, Montreal, Quebec, H3G 1M8, CANADA*

Received 1 March 2000; accepted 15 March 2000

Abstract

A high speed InGaAs/InP one-sided junction photodiode (OSJ-PD) with low junction capacitance is presented and investigated for the first time. Compared with the well known uni-traveling carrier photodiode (UTC-PD), the OSJ-PD has the advantages of simpler epitaxial layer structure and lower junction capacitance, while maintaining the characteristics of high speed and high output power. The OSJ-PD is studied by simulation. The performance characteristics of OSJ-PD including internal electric field distribution, energy band diagram, frequency response, photocurrent and junction capacitance, are carefully studied.

Keywords: InGaAs, InP, photodetector, one-sided junction photodiode, uni-traveling carrier photodiode.

1. Introduction

Photodiode is the key component for many applications, such as high speed fibre-optic communication systems [1], radio-over-fibre wireless communication systems [2-4], terahertz (THz) and millimetre-wave (MMW) generation schemes [5], etc. Thanks to the development of Erbium Doped Fibre Amplifier (EDFA), by combining high speed photodiode and powerful EDFA, THz and MMW signals can be generated directly from photonic links. Compared with other THz and MMW signal generation techniques [6], this approach can eliminate the need of bulky and expensive electrical post-amplifiers. Thus the overall bandwidth can be very broad, and the overall system complexity can be reduced. Moreover, photodiode can be integrated with photonic integrated circuit (PIC) components and even with a planar antenna for many applications [2,3,7,8].

Since photodiode is the main limitation for the overall performance of the aforementioned systems, there is an urgent need for high speed and high output power photodiodes. Before the invention of uni-traveling carrier photodiode (UTC-PD), PIN photodiode (PIN-PD) [9-14] has been used for fibre-optic communications, since it has a broad bandwidth of 67 GHz [9] and over 100 GHz [10,11]. However, for conventional PIN-PD, both holes and electrons are active carriers. Since the holes drift at a lower velocity, the performance of PIN-PD, such as bandwidth, is limited by holes. And thus there is an inevitable tradeoff between output power and other characteristics [11].

To overcome the inherent drawbacks of PIN-PD, UTC-PD was first developed in 1997 [15]. Since UTC-PD utilizes fast carrier electrons as the only active carriers, the speed and output power is improved significantly compared

with PIN-PD. In UTC-PD, the absorption layer and depletion layer are separated, which decouples the bandwidths determined by transit time and resistance-capacitance (RC) charging time. With the increasing demand of wireless communications, the MMW frequency range from 40 GHz to 300 GHz has attracted more and more attention [2,3]. MMW-over-fibre (MoF) technique is a promising solution for such wireless communication systems [2,3]. Nowadays, UTC-PD has been widely used for MoF links. It has been demonstrated that the UTC-PD at C-band wavelength range can have a bandwidth from 20 GHz to 315 GHz [16-24]. All UTC-PD structures, such as stepped doping [16,20,22] or linear-graded doping [17-19,21] in the absorption layer, modified UTC-PD (MUTC-PD) [16], triple transition region photodiode (TTR-PD) [24], and near-ballistic UTC-PD (NBUTC-PD) [17-19,21] have been proposed from the basic UTC-PD structure [15].

To simplify the epitaxial layer structure and improve the performance of photodiodes, we propose a high speed one-sided junction photodiode (OSJ-PD) with low junction capacitance, which can be an excellent photodiode for MoF links. The OSJ-PD is proposed based on the concept of the InGaAs Schottky barrier photodiode (SB-PD) [25-29] and UTC-PD [15]. However, since the Schottky barrier height of InGaAs is very low (about 0.2 to 0.3 eV), the dark current of InGaAs SBD is high [27]. This drawback has dramatically limited the applications of InGaAs SB-PD, and there are very few reports on it. Extensive studies have been conducted to overcome this drawback and different approaches have been adopted to increase the InGaAs Schottky barrier height. These approaches include cryogenic processing of metal deposition [30,31], chemical passivation [32], employing a thin cap layer of InAlAs, InP, Al₂O₃, GaAs or InGaP to increase barrier height [33-37],

* Corresponding author.

E-mail: xzhang@ece.concordia.ca

adding a thin counter-doped p^+ -InGaAs layer on n-InGaAs [37-39], etc. However, cryogenic processing and chemical passivation require additional fabrication steps and employing a thin cap layer will result in energy band discontinuity. Thus, a OSJ-PD structure has been adopted without complicating fabrication process and causing energy band discontinuity.

In this paper, the OSJ-PD is proposed and studied by theoretical analysis and Technology Computer-Aided Design (TCAD) simulation. The performance characteristics of UTC-PD and OSJ-PD are compared carefully. First, the epitaxial layer structures and the energy band diagrams of UTC-PD and OSJ-PD are illustrated. Then, the theory used for TCAD simulation is explained briefly. Finally, the simulated characteristics of UTC-PD and OSJ-PD including internal electric field distribution, energy band diagram, electron and hole concentration, electron and hole current, frequency response, photocurrent, and junction capacitance are presented and compared.

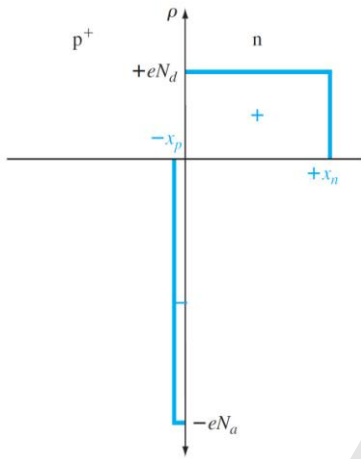


Fig. 1. Space charge density of a one-sided p^+n junction.

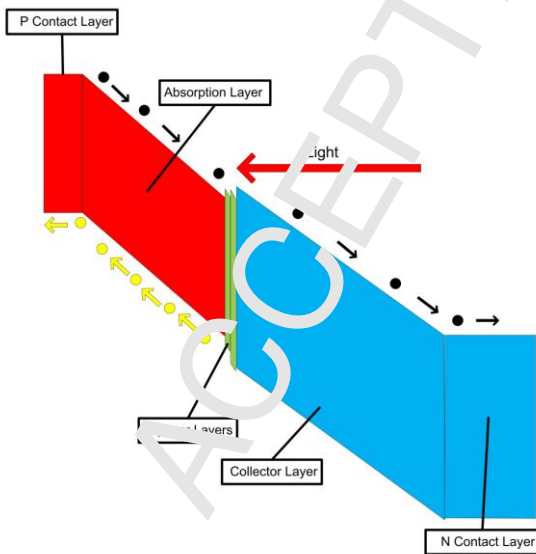


Fig. 2. Energy band diagram of OSJ-PD.

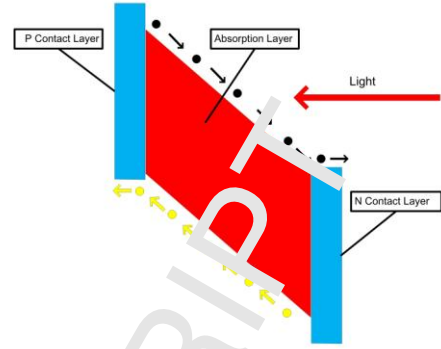


Fig. 3. Energy band diagram of PIN-PD.

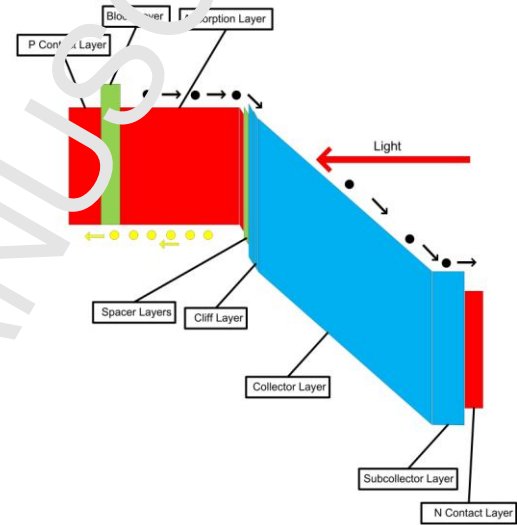


Fig. 4. Energy band diagram of UTC-PD.

2. Device design and operation

An asymmetrical pn junction is called a one-sided junction, either a p^+n junction or a n^+p junction, where p^+ and n^+ indicate heavily doped semiconductor. The schematic diagram of a p^+n junction is given in Fig. 1. For the p^+n junction, $x_p \ll x_n$ and $W \approx x_n$, where x_p is the depletion width in p^+ region, x_n is the depletion width in n region, and W is the total depletion width. The heavily doped semiconductor is similar to metal and there is no depletion in metal [40]. The OSJ-PD structure is similar to SB-PD structure [25-29], since the heavily doped p contact layer is similar to metal. The epitaxial layer structure of the designed OSJ-PD is given in Table 1. In order to make a comparison, the epitaxial layer structure of the conventional UTC-PD is given in Table 2. The detailed numerical modelling study of the conventional UTC-PD is given in [41]. Obviously, the OSJ-PD has a much simpler structure, which can lower the cost for epitaxial layer material growth.

The designed OSJ-PD is a backside illuminated photodiode, operating at around 1550 nm light wavelength.

From top to bottom, the OSJ-PD epitaxial layer structure consists of a heavily doped p-type InGaAs contact layer, a lightly doped n-type InGaAs absorption layer, two lightly doped n-type InGaAsP spacer layers, a lightly doped n-type InP collector layer and a heavily doped n-type InP contact

layer. This simple structure can be grown by Metal-organic Chemical Vapor Deposition (MOCVD) or Molecular beam epitaxy (MBE).

Table 1
Epitaxial layer structure of the OSJ-PD.

Layer	Material	Band gap (eV)	Thickness (nm)	Doping level (cm ⁻³)	Dopant type
P Contact	InGaAs	0.734	50	1×10^{19}	P
Absorption	InGaAs	0.734	300	5×10^{15}	N
Spacer	InGaAsP	0.882	20	5×10^{15}	N
Spacer	InGaAsP	1.105	20	5×10^{15}	N
Collector	InP	1.35	300	2×10^{16}	N
N Contact	InP	1.35	800	8×10^{18}	N

Table 2
Epitaxial layer structure of the UTC-PD.

Layer	Material	Band gap (eV)	Thickness (nm)	Doping level (cm ⁻³)	Dopant type
P Contact	InGaAs	0.73	50	3×10^{19}	P
Block	InGaAsP	0.85	20	2×10^{19}	P
Absorption	InGaAs	0.73	220	1×10^{18}	P
Spacer	InGaAs	0.73	8	1×10^{15}	Undoped
Spacer	InGaAsP	1.00	16	1×10^{15}	Undoped
Spacer	InP	1.35	6	1×10^{15}	Undoped
Cliff	InP	1.35	7	1×10^{18}	N
Collector	InP	1.35	263	1×10^{16}	N
Subcollector	InP	1.35	50	5×10^{18}	N
N Contact (Etch Stop)	InGaAs	0.73	10	1×10^{19}	N

Table 3
Material parameters used in the simulation.

Parameter	InP	InGaAs
Electron mobility, μ_n	54×10^4 cm ² /Vs	12000 cm ² /Vs
Hole mobility, μ_p	200 cm ² /Vs	300 cm ² /Vs
Conduction band density of states, N_c	5.7×10^{17} cm ⁻³	2.1×10^{17} cm ⁻³
Valence band density of states, N_v	1×10^{19} cm ⁻³	7.7×10^{18} cm ⁻³
Electron saturation velocity	2.6×10^7 cm/s	2.5×10^7 cm/s
Hole saturation velocity	5×10^6 cm/s	5×10^6 cm/s
Electron and hole life time (UTC-PD)	1×10^{-9} s	1×10^{-9} s
Electron and hole life time (OSJ-PD)	2×10^{-9} s	1×10^{-7} s
Electron Auger coefficient	3.7×10^{-31} cm ⁶ /s	3.2×10^{-28} cm ⁶ /s
Hole Auger coefficient	8.7×10^{-30} cm ⁶ /s	3.2×10^{-28} cm ⁶ /s
Real refractive index (1550 nm)	3.165	3.595
Imaginary refractive index (1550 nm)	0	0.075

Table 4
Mobility model parameters used in the simulation.

Mobility parameter	Parameter description	InP	InGaAs
MU1N.CAUGH	Maximum mobility at high doping	300 cm ² /Vs	3372 cm ² /Vs
MU2N.CAUGH	Maximum mobility at low doping	4917 cm ² /Vs	11599 cm ² /Vs
MU1P.CAUGH	Minimum mobility at high doping	20 cm ² /Vs	75 cm ² /Vs
MU2P.CAUGH	Maximum mobility at low doping	151 cm ² /Vs	331 cm ² /Vs
ALPHAN.CAUGH	Fitting parameter	0	0
ALPHAP.CAUGH	Fitting parameter	0	0
BETAN.CAUGH	Fitting parameter	-2.3	-2.3
BETAP.CAUGH	Fitting parameter	-2.2	-2.2
GAMMAN.CAUGH	Fitting parameter	-3.8	-3.8
GAMMAP.CAUGH	Fitting parameter	-3.7	-3.7
DELTAN.CAUGH	Fitting parameter	0.46	0.76
DELTAP.CAUGH	Fitting parameter	0.96	1.37
NCRITN.CAUGH	Critical doping above which mobility degrades	6.4×10^{17} cm ⁻³	8.9×10^{16} cm ⁻³
NCRITP.CAUGH	Critical doping above which mobility degrades	7.4×10^{17} cm ⁻³	1×10^{18} cm ⁻³

To better understand the operating mechanism and the advantages of the OSJ-PD, the energy band diagram of the OSJ-PD is given in Fig. 2. The energy band diagrams of the PIN-PD and UTC-PD are also given in Figs. 3 and 4 for comparison. Light is injected into the bottom N contact layer and passes through the collector layer, which is composed of wide energy gap material InP, and then absorbed in the absorption layer, which is composed of narrow energy gap material InGaAs. The electron and hole pairs are generated in the absorption layer and then separated and swept away quickly by the strong electric field in the absorption layer. This phenomenon differs significantly from the conventional UTC-PD [41], which utilizes electrons as the only active carriers. In the UTC-PD, electron and hole pairs are generated in the absorption layer, and minority carrier electrons will diffuse/drift to the collector layer. Since electrons' diffusive velocity in the absorption layer is usually lower than the drift velocity in the collector layer, the bandwidth of UTC-PD is mainly dominated and limited by electrons' traveling time in the absorption layer [42].

In the OSJ-PD, since all the active layers are depleted, the slow diffusion process can be eliminated. Both electrons and holes travel at saturation velocity or faster. The saturation velocities of electrons and holes in InGaAs are 2.5×10^7 cm/s and 5×10^6 cm/s respectively, and the saturation velocities of electrons and holes in InP are 2.6×10^7 cm/s and 6.6×10^6 cm/s respectively [42-45]. As shown in Fig. 2, the traveling distance of holes is much shorter than that of electrons. Even though the saturation velocity of holes is slower than that of electrons, the traveling time of electrons and holes can be tuned by carefully designing the thickness of an absorption layer and a collector layer. Generally speaking, the speed of a photodiode, i.e., 3-dB bandwidth, is mainly determined by,

$$f_{3dB} = \frac{1}{\sqrt{\tau_{tr}^2 + \tau_{RC}^2}} \quad (1)$$

where τ_{tr} is carrier transition time and τ_{RC} is RC charging time. The output power of a photodiode is mainly determined by space charge effect and thermal management. In OSJ-PD, since the absorption layer and collector layer are separated, the carrier transition time and RC charging time can be adjusted independently. Thus, the OSJ-PD can be designed with a comparable bandwidth to UTC-PD. Because the OSJ-PD is reversely biased at high voltage and the internal electric field is high, the space charge effect can be reduced well, and thus high output power is achievable.

3. Physics models for TCAD simulation

TCAD simulation is used to design and analyze UTC-PD and OSJ-PD. The physics-based device simulator ATLAS has been used to predict the device performance and provide a deep insight view into the physics of device operation [46]. Device characteristics are obtained by

solving the Poisson's equation (2), the transport equation (3) and the continuity equation (4) of electrons and holes [46].

$$\nabla^2 \psi = -\frac{\rho}{\epsilon} \quad (2)$$

$$\begin{aligned} \bar{J}_n &= q\mu_n n \bar{E} + qD_n \bar{\nabla} n \\ \bar{J}_p &= q\mu_p p \bar{E} - qD_p \bar{\nabla} p \end{aligned} \quad (3)$$

$$\begin{aligned} \frac{\partial n}{\partial t} &= G_n - R_n + \frac{1}{q} \nabla \cdot \bar{J}_n \\ \frac{\partial p}{\partial t} &= G_p - R_p - \frac{1}{q} \nabla \cdot \bar{J}_p \end{aligned} \quad (4)$$

ψ is the electrostatic potential, ϵ is the permittivity, ρ is the space charge density, \bar{J}_n and \bar{J}_p are the electron and the hole current densities, μ_n and μ_p are electron and hole mobility, D_n and D_p are electron and hole diffusion coefficients, q is electron charge, G_n and G_p are electron and hole generation rates and R_n and R_p are electron and hole recombination rates.

The electrical and optical properties of InGaAs and InP materials are taken from [43-45,47-51] and the parameters used in our simulation are given in Tables 3 and 4. Basic models included in TCAD simulation are: concentration-dependent lifetime model CONSRH, concentration-dependent mobility model ANALYTIC, parallel electric field dependent mobility model FLDMOB, Shockley-Read-Hall recombination minority carrier lifetime model SRH, and Auger recombination model AUGER. In order to verify the accuracy of our simulation models and configurations, we have compared our simulation results with [41,47] and similar results can be reproduced. To make the simulated results comparable, all devices' area is set to $20 \mu\text{m}^2$ and load resistance is set to 50Ω . Excluding contact layers, the UTC-PD has a thickness of 590 nm and the OSJ-PD has a comparable thickness of 640 nm.

4. Device characteristics

4.1 Reverse bias voltage and internal electric field

Photodiode serves as an O/E converter. In order to get high output, reverse bias voltage should always be applied. However, a high reverse bias voltage could result in device breakdown. The breakdown electric fields of InGaAs and InP are around 2×10^5 V/cm and 5×10^5 V/cm respectively [50]. In conventional UTC-PD given in Table 2, the depletion region is the spacer layers, cliff layer, and collector layer. The total depletion width is around 300 nm. As shown in Fig. 5, at bias voltages of -2 V and -4 V, the

electric fields in spacer and cliff layers are around 200 kV/cm and 250 kV/cm respectively, and the electric fields in collector layer are around 100 kV/cm and 150 kV/cm respectively.

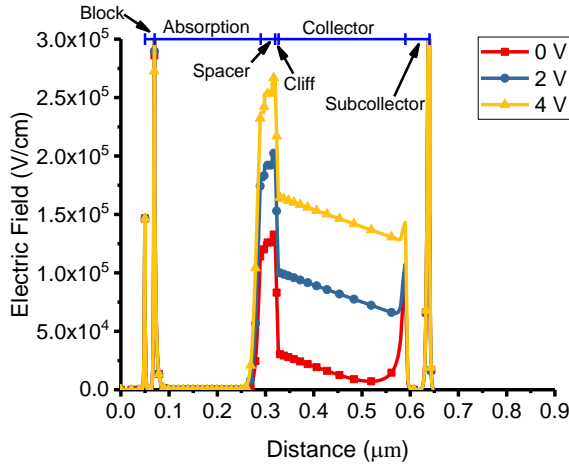


Fig. 5. Internal electric field distribution of UTC-PD with reverse bias voltage of 0, 2 and 4 V.

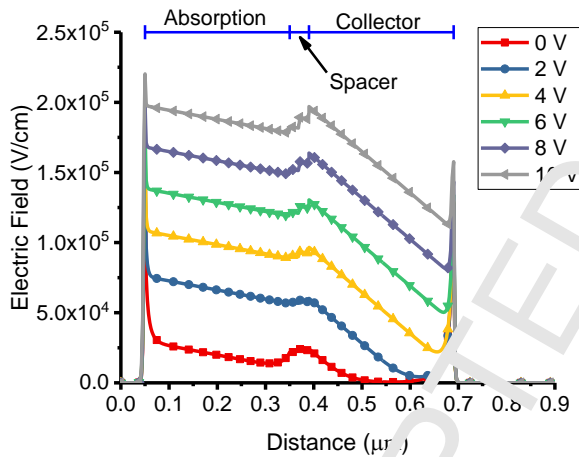


Fig. 6. Internal electric field distribution of OSJ-PD with reverse bias voltage of 0, 2, 4, 6, 8 and 10 V.

For OSJ-PD, the situation is completely different. Since all the active layers are depleted, a large reverse bias voltage can be applied without causing device breakdown. The internal electric field of OSJ-PD simulated at bias voltage of 0, 2, 4, 6, 8 and 10 V is shown in Fig. 6. The one-sided junction structure (similar to Schottky diode, since heavily doped contact layer is similar to metal.) can produce a 25 kV/cm built-in electric field in the absorption layer without any bias voltage. At high reverse bias voltage of 10 V, the maximum internal electric field is around 200 kV/cm. Since the depletion width is very large, about 640 nm, the device cannot be broken-down even at a large reverse bias voltage of 10 V. And large bias voltage can

produce higher output current. Thus OSJ-PD is suitable for applications which require high RF output power.

4.2 Energy band diagram

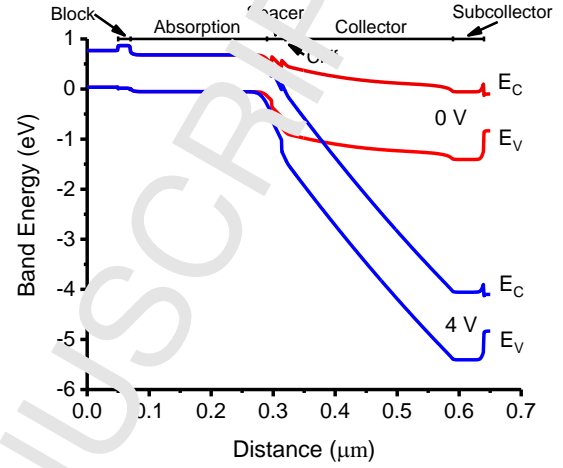


Fig. 7. Simulated energy band diagram of conventional UTC-PD with reverse bias voltage of 0 V and 4 V.

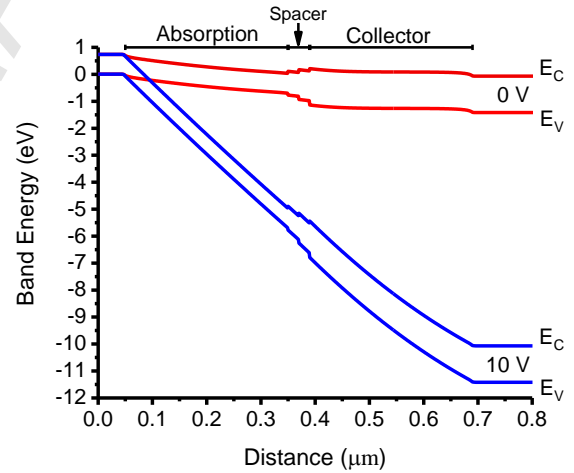


Fig. 8. Simulated energy band diagram of OSJ-PD with reverse bias voltage of 0 V and 10 V.

The energy band diagrams of UTC-PD (Table 2) and OSJ-PD (Table 1) with and without reverse bias voltage are given in Figs. 7 and 8. Obviously, the operation mechanisms of UTC-PD and OSJ-PD are different. In UTC-PD, the electric field in absorption layer is almost zero and a block layer is used to prevent the photogenerated electrons from diffusing towards contact layer. In OSJ-PD, the electric field in absorption layer is strong enough and photogenerated electron and hole pairs will be swept out of the depletion region quickly. Thus, there is no need for a block layer, which is necessary for conventional UTC-PD. Electrons and holes will drift towards n and p contact layers respectively. This feature differs significantly from the conventional UTC-PD and greatly simplifies the epitaxial

layer structure. In UTC-PD, a cliff layer is used to increase the electric field and facilitate the traveling of electrons at the interface between absorption layer and collector layer. In OSJ-PD, the electric field is too high so that electrons can travel through spacer layers easily even without a cliff layer.

4.3 Electron and hole concentration

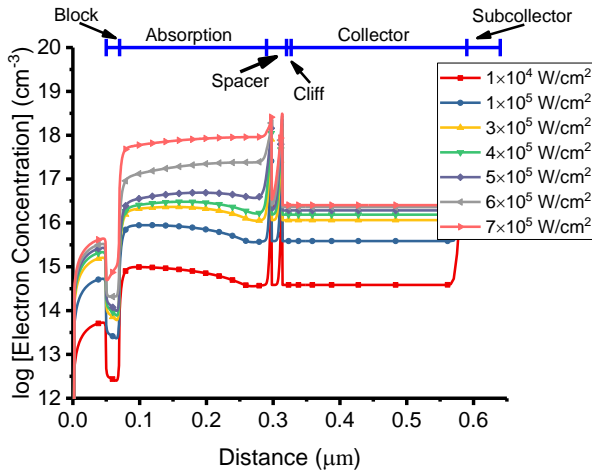


Fig. 9. Electron concentration profiles of UTC-PD with 4 V reverse bias voltage at different light intensities.

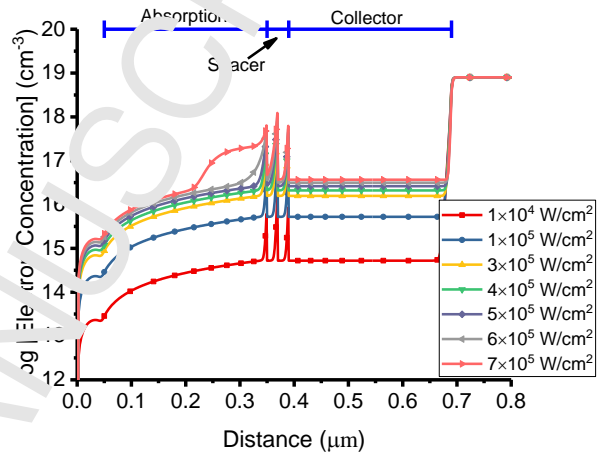


Fig. 11. Electron concentration profiles of OSJ-PD with 10 V reverse bias voltage at different light intensities.

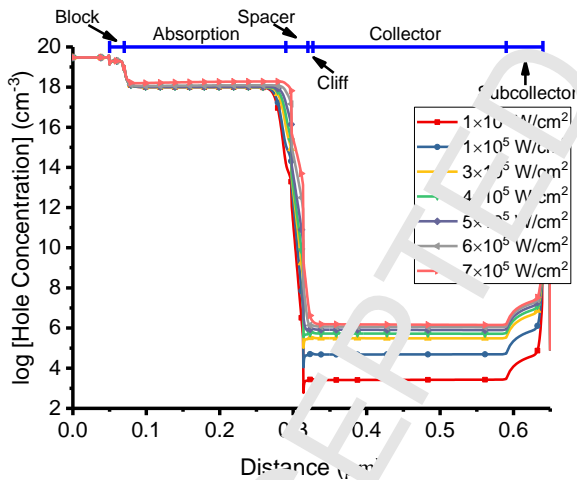


Fig. 10. Hole concentration profiles of UTC-PD with 4 V reverse bias voltage at different light intensities.

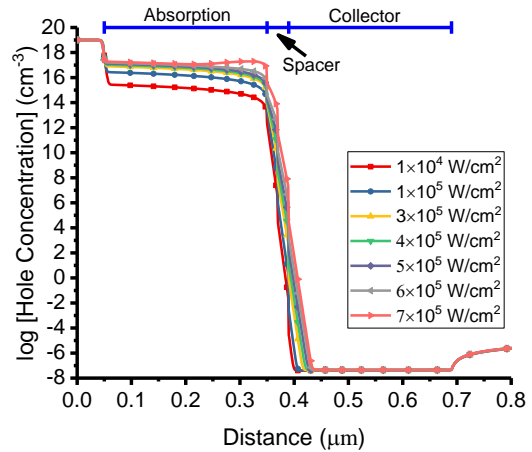


Fig. 12. Hole concentration profiles of OSJ-PD with 10 V reverse bias voltage at different light intensities.

For UTC-PD, the electron and hole concentration profiles across the device are given in Figs. 9 and 10. Light is absorbed in the absorption layer and electron and hole pairs are generated in this layer. Photogenerated electrons diffuse towards spacer layers and then drift through spacer and collector layers under high electric field. As shown in Fig. 9, electron concentration across the device increases with injected light intensity. However, the electron concentration in collector layer stops to increase when light intensity goes beyond $5 \times 10^5 \text{ W/cm}^2$. Large amount of

electrons begin to accumulate in absorption layer and saturation occurs. Since holes are majority carriers in heavily doped p-type absorption layer, photogenerated holes respond very fast within the dielectric relaxation time and excess holes will return to equilibrium by conduction process. As shown in Fig. 10, the hole concentration across the device is almost constant at different light intensities. The variation of hole concentration in the collector layer is mainly due to light absorption in the 10 nm InGaAs contact (etch stop) layer. Therefore, the photoresponse of a UTC-PD is mainly determined by electron transportation.

For OSJ-PD, the electron and hole concentration profiles across the device are given in Figs. 11 and 12. The absorption layer is totally depleted. Photogenerated electron and hole pairs are separated by internal electric field and electrons and holes drift towards n-type and p-type contact layers respectively. The photoresponse of a OSJ-PD is determined by both electrons and holes, which is significantly different from a UTC-PD. Thanks to the shorter traveling distance of holes, though holes travel at a

relatively low saturation velocity of 5×10^6 cm/s, they won't slow down the overall speed. As shown in Fig. 11, the electron concentration increases with injected light intensity. However, electrons in the absorption layer start to accumulate when light intensity reaches 6×10^5 W/cm² and electron concentration in the collector layer stops to increase. As shown in Fig. 12, the hole concentration across the device is almost constant at different light intensities, except in the absorption layer. In the absorption layer, hole concentration increases with injected light intensity. Obviously, hole accumulation doesn't occur from a low light intensity of 1×10^4 W/cm² to a high light intensity of 6×10^5 W/cm². Holes start to accumulate near the interface between absorption layer and spacer layer at a light intensity of 7×10^5 W/cm². At high light intensity, not only holes but also electrons accumulate. The electrons accumulation is mainly caused by conduction band discontinuity between InGaAs and InP. When large amount of electrons accumulate, the internal electric field starts to drop. Once internal electric field drops to below 40 kV/cm, the traveling velocity of holes starts to decrease and holes accumulation occurs. Since there isn't any valence band discontinuity between p contact layer and absorption layer, holes can travel easily from absorption layer to p contact layer and holes accumulation is not prominent.

4.4 Electron and hole current

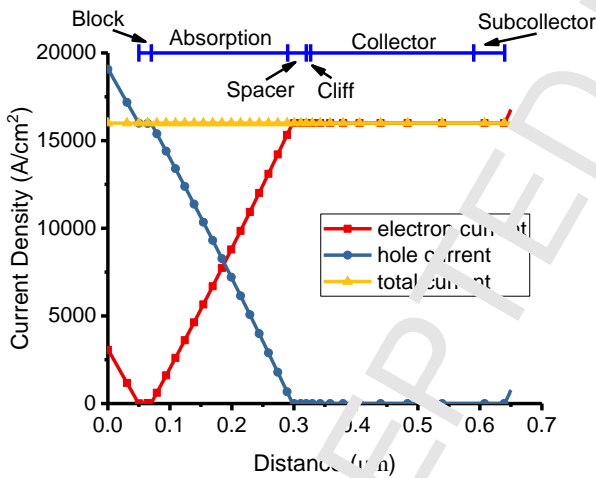


Fig. 13. Electron, hole and total current density inside the UTC-PD with 4 V reverse bias voltage at light intensity of 1×10^5 W/cm².

Fig. 13 shows the electron, hole and total current density inside the UTC-PD. In the absorption layer, both electrons and holes contribute to the photocurrent. Electrons diffuse towards the collector layer and holes drift to the p contact layer. The electron current increases from zero at the block layer interface to maximum at the spacer layer interface. The hole current increases from zero at the spacer layer interface to maximum at the block layer interface. In the collector layer, the photocurrent is carried totally by electrons drifting towards n contact layer. The total current across the device is constant since the photodiode is a two

terminal device. Note that light might be absorbed in the p contact layer also. In the p contact layer, since holes drift towards metal and electrons diffuse towards metal also, they cancel each other and the total current doesn't change.

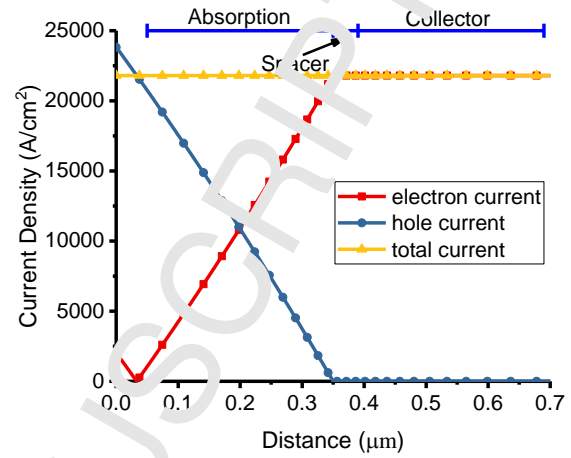


Fig. 14. Electron, hole and total current density inside the OSJ-PD with 10 V reverse bias voltage at light intensity of 1×10^5 W/cm².

For OSJ-PD, the electron, hole and total current density inside the device is given in Fig. 14, which is similar to UTC-PD. The main difference is inside the absorption layer, which is fully depleted. In OSJ-PD, Electrons drift instead of diffusing towards collector layer and holes drift under high electric field instead of drifting as majority carrier towards p contact layer.

4.5 Internal electric field at different light intensities

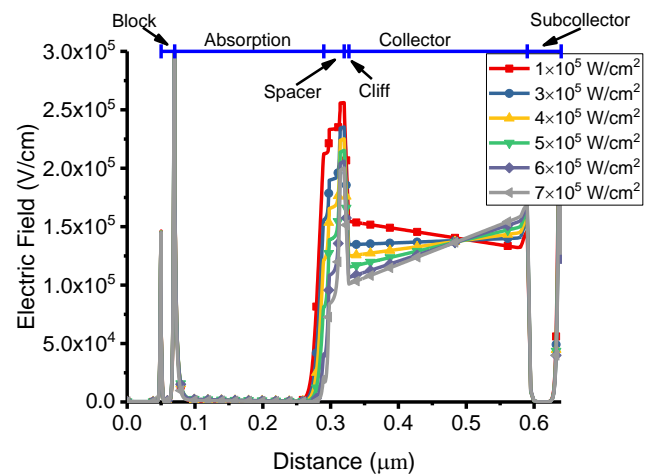


Fig. 15. Internal electric field of UTC-PD with 4 V reverse bias voltage at different light intensities.

The internal electric field of UTC-PD with 4 V reverse bias voltage versus different injected light intensities is given in Fig. 15. When light intensity reaches 5×10^5 W/cm², the electric field at the interface of absorption layer and spacer layers drops to zero and electrons start to

accumulate. It agrees well with the phenomenon in Fig. 9 that electron concentration in collector layer doesn't increase with injected light intensity when it goes beyond $5 \times 10^5 \text{ W/cm}^2$.

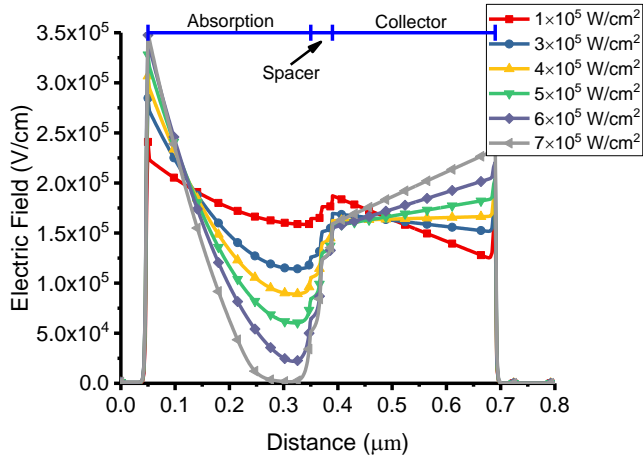


Fig. 16. Internal electric field of OSJ-PD with 10 V reverse bias voltage at different light intensities.

The internal electric field of OSJ-PD with 10 V reverse bias voltage versus different injected light intensities is given in Fig. 16. When light intensity reaches $6 \times 10^5 \text{ W/cm}^2$, the electric field at the interface of absorption layer and spacer layers drops to below 40 kV/cm and both electrons and holes start to accumulate. It agrees well with the phenomenon in Fig. 11 that electron concentration in collector layer doesn't increase with injected light intensity when it goes beyond $6 \times 10^5 \text{ W/cm}^2$.

4.6 Frequency response

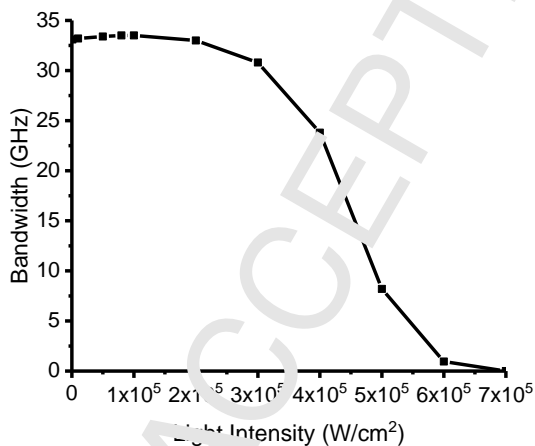


Fig. 17. Simulated 3-dB bandwidth of UTC-PD versus light intensity.

The frequency responses of UTC-PD and OSJ-PD are obtained by small signal analysis in TCAD simulation and are given in Figs. 17 and 18. For both UTC-PD and OSJ-PD, because of the space charge effect the 3-dB bandwidth

drops when injected light intensity increases. However, their mechanisms for bandwidth degradation are different. For UTC-PD, electrons are driven by concentration gradient in the absorption layer. As shown in Fig. 9, electron concentration gradient is prominent when light intensity is below $4 \times 10^5 \text{ W/cm}^2$ and the gradient vanishes at light intensities above $5 \times 10^5 \text{ W/cm}^2$. The variation of electron concentration gradient in Fig. 9 agrees well with the change of 3-dB bandwidth in Fig. 17. For OSJ-PD, both electrons and holes are driven by internal electric field. As shown in Fig. 16, the internal electric field drops to zero at light intensity of $7 \times 10^5 \text{ W/cm}^2$. The variation of internal electric field in Fig. 16 corresponds well with the change of 3-dB bandwidth in Fig. 18.

As shown in Figs. 17 and 18, the UTC-PD with 220 nm absorption layer and 263 nm collector layer has a bandwidth of 33.5 GHz at low light intensity, while the OSJ-PD with 500 nm absorption layer and 300 nm collector layer has a bandwidth of 64 GHz at low light intensity.

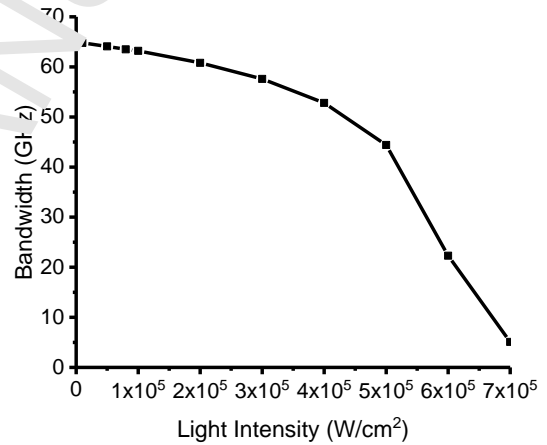


Fig. 18. Simulated 3-dB bandwidth of OSJ-PD versus light intensity.

4.7 Photocurrent

The simulated DC photocurrent densities of the UTC-PD and OSJ-PD versus injected light intensity with different bias voltage are given in Figs. 19 and 20. The UTC-PD can achieve a photocurrent density of more than $1.1 \times 10^5 \text{ A/cm}^2$ with a bias voltage of 4 V. The OSJ-PD can achieve a photocurrent density of more than $2.4 \times 10^5 \text{ A/cm}^2$ with a bias voltage of 10 V. In reality, the maximum current density can be improved by thermal management, i.e., flip-chip bonding the photodiode onto high thermal conductive substrate such as AlN or Diamond [17-19,21,23]. Obviously, the reverse bias voltage has a great influence on the photocurrent and photocurrent density usually increases with bias voltage. However, the bias voltage should be lower than the breakdown voltage of the device. Mainly due to the much higher bias voltage, the saturation photocurrent of OSJ-PD is much higher than UTC-PD. It's worth mentioning that the space charge effect

in UTC-PD and OSJ-PD can be relaxed by modified uni-traveling carrier photodiode (MUTC-PD) structure and modified one-sided junction photodiode (OSJ-PD) structure respectively. And the detailed discussion can be found in [16,52].

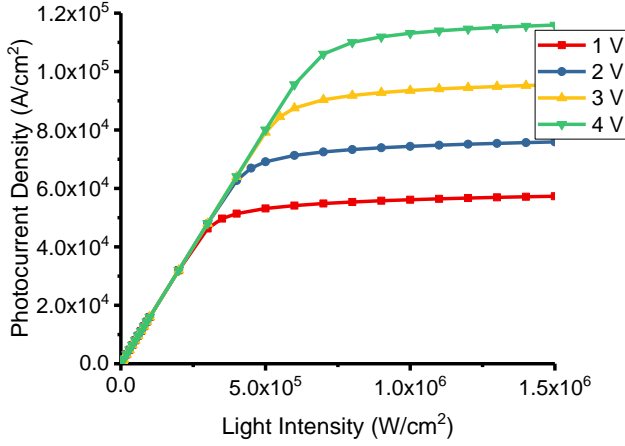


Fig. 19. Simulated DC photocurrent density versus light intensity with different reverse bias voltage (UTC-PD).

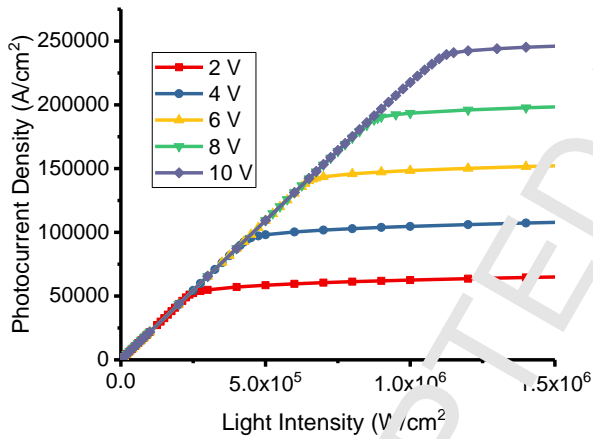


Fig. 20. Simulated DC photocurrent density versus light intensity with different reverse bias voltage (OSJ-PD).

4.8 Junction capacitance

Since the overall speed of the photodiode is determined by transit time and RC charging time (1), another effective way to improve speed is to reduce the RC charging time. The RC charging time can be expressed as,

$$\tau_{RC} = 2\pi(R_s + R_l)(C_j + C_p) \quad (5)$$

where R_s , R_l , C_j , and C_p are series resistance, load resistance, junction capacitance and parasitic capacitance respectively. Photodiode with a lower junction capacitance can relax the bandwidth degradation caused by RC

charging time. The photodiode junction capacitance is similar to parallel plate capacitance, which is given by

$$C = \frac{\epsilon_r \epsilon_0 A}{d} \quad (6)$$

where ϵ_r , ϵ_0 , A and d are relative permittivity, permittivity of free space, area of the junction and depletion width, respectively. Since the photodiode has multilayer dielectric, the equivalent permittivity is given by [53],

$$\epsilon_{req} = \left[\sum_{m=1}^n \frac{d_m}{d_T \epsilon_{rm}} \right]^{-1} \quad (7)$$

$$d_T = d_1 + d_2 + \dots + d_n \quad (8)$$

where d_m is the thickness and ϵ_{rm} is the relative permittivity of the m -th layer dielectric, and d_T is the total thickness. In UTC-PD, the depletion region is the spacer layers, cliff layer, and collector layer. In OSJ-PD, the depleted region is the absorption layer, spacer layers, and collector layer. Since the depletion width of OSJ-PD is usually larger than UTC-PD, for device with the same area, the junction capacitance of OSJ-PD can be lower than UTC-PD.

5. Conclusion

We have proposed a novel concept, one-sided junction photodiode, for InGaAs/InP photodiode design. The concept of OSJ-PD is different from the UTC-PD in the epitaxial layer structure, internal electric field distribution, energy band diagram and operation mechanism. It has been demonstrated that the OSJ-PD has the characteristics of the simple epitaxial layer structure, high speed, high output power, and low junction capacitance. The OSJ-PD with 300 nm absorption layer thickness has achieved a bandwidth of 64 GHz and a photocurrent density of 2.4×10^5 A/cm² under a 10 V bias voltage. The OSJ-PD can become an attractive choice for high speed fibre-optic communication systems, radio-over-fibre wireless communication systems, and THz and MMW generation schemes in the future.

Acknowledgements

This work has been worked by FRQNT team research project of Quebec.

References

- [1] K. Fukuchi, T. Kasamatsu, M. Morie, R. Ohhira, T. Ito, K. Sekiya, D. Ogasahara, T. Ono, 10.92-Tb/s (273 x 40-Gb/s) triple-band/ultra-dense WDM optical-repeated transmission experiment, Optical Fiber Communication Conference and International Conference on Quantum Information (2001), Paper PD24, Optical Society of America, 2001: p. PD24. <https://doi.org/10.1364/OFC.2001.PD24>.
- [2] J.-W. Shi, C.-B. Huang, C.-L. Pan, Millimeter-wave photonic wireless links for very high data rate communication, NPG Asia Mater. 3 (2011) 41–48. <https://doi.org/10.1038/asiamat.2010.193>.
- [3] S. Koenig, D. Lopez-Diaz, J. Antes, F. Boes, R. Henneberger, A. Leuther, A. Tessmann, R. Schmogrow, D. Hillerkuss, R. Palmer, T.

- Zwick, C. Koos, W. Freude, O. Ambacher, J. Leuthold, I. Kallfass, Wireless sub-THz communication system with high data rate, *Nat. Photonics*. 7 (2013) 977–981. <https://doi.org/10.1038/nphoton.2013.275>.
- [4] H.J. Song, T. Nagatsuma, Present and Future of Terahertz Communications, *IEEE Trans. Terahertz Sci. Technol.* 1 (2011) 256–263. <https://doi.org/10.1109/TTTHZ.2011.2159552>.
- [5] A.J. Seeds, K.J. Williams, Microwave Photonics, *J. Lightwave Technol.* 24 (2006) 4628–4641. <https://doi.org/10.1109/JLT.2006.885787>.
- [6] G. Chattopadhyay, Technology, Capabilities, and Performance of Low Power Terahertz Sources, *IEEE Trans. Terahertz Sci. Technol.* 1 (2011) 33–53. <https://doi.org/10.1109/TTTHZ.2011.2159561>.
- [7] H. Ito, S. Kodama, Y. Muramoto, T. Furuta, T. Nagatsuma, T. Ishibashi, High-speed and high-output InP-InGaAs untraveling-carrier photodiodes, *IEEE J. Sel. Top. Quantum Electron.* 10 (2004) 709–727. <https://doi.org/10.1109/JSTQE.2004.833883>.
- [8] H. Ito, T. Furuta, Y. Hirota, T. Ishibashi, A. Hirata, T. Nagatsuma, H. Matsuo, T. Noguchi, M. Ishiguro, Photonic millimetre-wave emission at 300 GHz using an antenna-integrated uni-travelling-carrier photodiode, *Electron. Lett.* 38 (2002) 989–990. <https://doi.org/10.1049/el:20020667>.
- [9] R.S. Tucker, A.J. Taylor, C.A. Burrus, G. Eisenstein, J.M. Wiesenfeld, Coaxially mounted 67 GHz bandwidth InGaAs PIN photodiode, *Electron. Lett.* 22 (1986) 917–918. <https://doi.org/10.1049/el:19860625>.
- [10] D. G. Parker, The theory, fabrication and assessment of ultra high speed photodiodes, *GEC J. Res.* 6 (1988) 106–117.
- [11] K. Kato, S. Hata, K. Kawano, A. Kozen, Design of Ultrawide-Band, High-Sensitivity p-i-n Photodetectors, *IEICE Trans. Electron.* E76–C (1993) 214–221.
- [12] T.-P. Lee, C. Burrus, A. Dentai, InGaAs/InP p-i-n photodiodes for lightwave communications at the 0.95–1.65 μm wavelength, *IEEE J. of Quantum Electron.* 17 (1981) 232–238. <https://doi.org/10.1109/JQE.1981.1071055>.
- [13] K. Li, E. Rezek, H.D. Law, InGaAs pin photodiode fabricated on semi-insulating InP substrate for monolithic integration, *Electron. Lett.* 20 (1984) 196–198. <https://doi.org/10.1049/el:19840130>.
- [14] M. Makiuchi, M. Norimatsu, C. Sakurai, K. Kondo, N. Yamamoto, M. Yano, Flip-chip planar GaInAs/InP p-i-n photodiodes-fabrication and characteristics, *J. Lightwave Technol.* 13 (1995) 2270–2275. <https://doi.org/10.1109/50.482047>.
- [15] T. Ishibashi, N. Shimizu, S. Kodama, H. Ito, T. Nagatsuma, and T. Furuta, Uni-travelling-carrier photodiodes, *Tech.Dig.Ultrafast Electron.Optoelectron.* (1997), paper UC3, pp. 166–173.
- [16] Z. Li, H. Pan, H. Chen, A. Beling, J.C. Campbell, High-Saturation-Current Modified Uni-Traveling-Carrier Photodiode With a Cliff Layer, *IEEE J. Quantum Electron.* 46 (2010) 626–632. <https://doi.org/10.1109/JQE.2010.2046140>.
- [17] J.W. Shi, F.M. Kuo, M.Z. Chou, A linear cascade near-ballistic untraveling-carrier photodiodes with extremely high saturation-current bandwidth product (6825mA-GHz, 75mA/1GHz) under a 50 Ω load, *Optical Fiber Communication*, 2010: pp. 1–3. <https://doi.org/10.1364/OFC.2010.PDPA6>.
- [18] Y.S. Wu, J.W. Shi, Dynamic Analysis of High-Power and High-Speed Near-Ballistic Untraveling Carrier Photodiodes at W-Band, *IEEE Photonics Technol. Lett.* 20 (2008) 1160–1162. <https://doi.org/10.1109/LPT.2008.925155>.
- [19] J.W. Shi, F.M. Kuo, C.J. Wu, C.L. Cheng, C.Y. Liu, C.Y. Chen, J.I. Chyi, Extremely High Saturation Current Bandwidth Product Performance of a Near-Ballistic Uni-Traveling-Carrier Photodiode With a Flip-Chip Bonding Structure, *IEEE J. Quantum Electron.* 46 (2010) 80–86. <https://doi.org/10.1109/JQE.2009.2027339>.
- [20] N. Shimizu, N. Watanabe, T. Furuta, T. Ishibashi, InP-InGaAs untraveling-carrier photodiode with improved 3-dB bandwidth of over 150 GHz, *IEEE Photonics Technol. Lett.* 10 (1998) 412–414. <https://doi.org/10.1109/50.730027>.
- [21] J.M. Wun, C.H. Lai, N.W. Chen, J.E. Bowers, J.W. Shi, Flip-Chip Bonding Packaged THz Photodiode With Broadband High-Power Performance, *IEEE Photonics Technol. Lett.* 26 (2014) 2462–2464. <https://doi.org/10.1109/LPT.2014.2358843>.
- [22] H. Ito, T. Furuta, S. Kodama, T. Ishibashi, InP/InGaAs uni-travelling-carrier photodiode with 310 GHz bandwidth, *Electron. Lett.* 36 (2000) 1809–1810. <https://doi.org/10.1049/el:20001274>.
- [23] J.-W. Shi, C.-L. Pan, C.-B. Huang, J.-M. Wun, H.-Y. Liu, Y.-L. Zeng, High-Power THz-Wave Generation by Using Ultra-Fast (315 GHz) Uni-Traveling Carrier Photodiode with Novel Collector Design and Photonic Femtosecond Pulse Generator, *Optical Fiber Communication Conference (2015), Paper M3C.6*, Optical Society of America, 2015: p. M3C.6. <https://doi.org/10.1364/OFC.2015.M3C.6>.
- [24] V. Rymanov, A. Stöhr, S. Dülmeier, T. A. Schmitt, Triple transit region photodiodes (TTR-PDs) providing high millimeter wave output power, *Opt. Express*. 22 (2014) 7550–7556. <https://doi.org/10.1364/OE.22.007550>.
- [25] A. Davidson, K. L. Dessau, Photodiode-based detector operates at 60 GHz. http://assets.newport.com/web_documents-EN/images/Photodiode-Based_Detector.PDF, Undated (accessed Feb. 2018).
- [26] S.-P. Han, H. Ko, J. W. Park, S. Kim, Y.-J. Yoon, J.-H. Shin, D.Y. Kim, D.H. Lee, K.H. Park, InGaAs Schottky barrier diode array detector for a real-time compact terahertz line scanner, *Opt. Express*. 21 (2013) 25874–25882. <https://doi.org/10.1364/OE.21.025874>.
- [27] S.S. Li, Development of a high speed InGaAs/InP Schottky barrier photodetector for millimeter-wave fiber optical links. <https://apps.dtic.mil/dtic/tr/fulltext/u2/a188594.pdf>, 1987 (accessed Oct. 2018).
- [28] N. Eme, H. Schuracher, H. Beneking, High-speed GaInAs Schottky photodetector, *Electron. Lett.* 21 (1985) 180–181. <https://doi.org/10.1049/el:19850127>.
- [29] J.-H. Kim, S.-J. Li, L. Figueroa, T.F. Carruthers, R.S. Wagner, High-speed Ga_{0.47}In_{0.53}As/InP infra-red Schottky-barrier photodiodes, *Electron. Lett.* 24 (1988) 1067–1068.
- [30] L. Li, M.J. Costello, K.Y. Cheng, D.E. Wohlert, Enhanced Schottky barrier InGaAs for high performance photodetector application, *J. Vac. Sci. Technol., A*. 16 (1998) 1646–1649. <https://doi.org/10.1116/1.581135>.
- [31] J.-H. Lee, W.A. Anderson, H. Hardtdegen, H. Lüth, Barrier height enhancement of Schottky diodes on n-In_{0.53}Ga_{0.47}As by cryogenic processing, *Appl. Phys. Lett.* 63 (1993) 1939–1941. <https://doi.org/10.1063/1.110607>.
- [32] K.C. Hwang, S.S. Li, C. Park, T.J. Anderson, Schottky barrier height enhancement of n-In_{0.53}Ga_{0.47}As by a novel chemical passivation technique, *J. Appl. Phys.* 67 (1990) 6571–6573. <https://doi.org/10.1063/1.345138>.
- [33] J.B.D. Soole, H. Schumacher, H.P. LeBlanc, R. Bhat, M.A. Koza, High-speed performance of OMCVD grown InAlAs/InGaAs MSM photodetectors at 1.5 μm and 1.3 μm wavelengths, *IEEE Photonics Technol. Lett.* 1 (1989) 250–252. <https://doi.org/10.1109/68.36058>.
- [34] J.B.D. Soole, H. Schumacher, InGaAs metal-semiconductor-metal photodetectors for long wavelength optical communications, *IEEE J. Quantum Electron.* 27 (1991) 737–752. <https://doi.org/10.1109/3.81384>.
- [35] D. Kuhl, F. Hieronymi, E.H. Botcher, T. Wolf, A. Krost, D. Bimberg, Very high-speed metal-semiconductor-metal InGaAs : Fe photodetectors with InP : Fe barrier enhancement layer grown by low pressure metalorganic chemical vapour deposition, *Electron. Lett.* 26 (1990) 2107–2109. <https://doi.org/10.1049/el:19901356>.
- [36] R. Wang, M. Xu, P.D. Ye, R. Huang, Schottky-barrier height modulation of metal/In_{0.53}Ga_{0.47}As interfaces by insertion of atomic-layer deposited ultrathin Al₂O₃, *J. Vac. Sci. Technol. B*. 29 (2011) 041206. <https://doi.org/10.1116/1.3610972>.
- [37] P. Kordoš, M. Marso, R. Meyer, H. Lüth, Schottky barrier height enhancement on n-In_{0.53}Ga_{0.47}As, *J. Appl. Phys.* 72 (1992) 2347–2355. <https://doi.org/10.1063/1.351576>.
- [38] C.Y. Chen, A.Y. Cho, K.Y. Cheng, P.A. Garbinski, Quasi-Schottky barrier diode on n-Ga_{0.47}In_{0.53}As using a fully depleted p+-Ga_{0.47}In_{0.53}As layer grown by molecular beam epitaxy, *Appl. Phys. Lett.* 40 (1982) 401–403. <https://doi.org/10.1063/1.93117>.
- [39] P. Kordos, M. Marso, R. Meyer, H. Lüth, Schottky contacts on n-In_{0.53}Ga_{0.47}As with enhanced barriers by counter-doped interfacial layers, *IEEE Trans. Electron Devices*. 39 (1992) 1970–1972. <https://doi.org/10.1109/16.144693>.
- [40] C. Hu, *Modern Semiconductor Devices for Integrated Circuits*, Prentice Hall, 2010.
- [41] S. Srivastava, K.P. Roenker, Numerical modeling study of the InP/InGaAs uni-travelling carrier photodiode, *Solid-State Electron.* 48 (2004) 461–470. <https://doi.org/10.1016/j.sse.2003.08.004>.

- 1 [42] T. Ishibashi, T. Furuta, H. Fushimi, S. Kodama, H. Ito, T. Nagatsuma,
2 N. Shimizu, Y. Miyamoto, InP/InGaAs Uni-Traveling-Carrier
3 Photodiodes, IEICE Trans. Electron. E83–C (2000) 938–949.
4 [43] S. Adachi, Physical Properties of III–V Semiconductor Compounds:
5 InP, InAs, GaAs, GaP, InGaAs and InGaAsP, 1 edition, Wiley
6 Interscience, New York, 1992.
7 [44] J.W. Parks, A.W. Smith, K.F. Brennan, L.E. Tarof, Theoretical study
8 of device sensitivity and gain saturation of separate absorption,
9 grading, charge, and multiplication InP/InGaAs avalanche
10 photodiodes, IEEE Trans. Electron Devices. 43 (1996) 2113–2121.
11 <https://doi.org/10.1109/16.544382>.
12 [45] S. Datta, S. Shi, K.P. Roenker, M.M. Cahay, W.E. Stanchina,
13 Simulation and design of InAlAs/InGaAs pnp heterojunction bipolar
14 transistors, IEEE Trans. Electron Devices. 45 (1998) 1634–1643.
15 <https://doi.org/10.1109/16.704357>.
16 [46] ATLAS Users Manual, Silvaco International, Santa Clara, 2013.
17 [47] S. Srivastava, Simulation study of InP-based uni-traveling carrier
18 photodiode (Master's Thesis), University of Cincinnati, 2003.
19 [48] P.A. Balaraman, Design, simulation and modeling of
20 InP/GaAsSb/InP double heterojunction bipolar transistors (Master's
21 Thesis), University of Cincinnati, 2003.
22 [49] Y.R. Shrestha, Numerical simulation of GaAsSb/InP uni-traveling
23 carrier photodiode (Master's Thesis), University of Cincinnati, 2005.
24 [50] New semiconductor materials, characteristics and properties,
25 <http://www.ioffe.rssi.ru/SVA/NSM/> (accessed Feb. 2018).
26 [51] R.K. Ahrenkiel, R. Ellingson, S. Johnston, J. Wanlass,
27 Recombination lifetime of In_{0.5}Ga_{0.5}As as a function of doping
28 density, Appl. Phys. Lett. 72 (1998) 3470–3472.
29 <https://doi.org/10.1063/1.1216000>.
30 [52] J. Xu, X. Zhang, A. Kish, Design of modified InGaAs/InP one-sided
31 junction photodiodes with improved response at high light intensity,
32 Appl. Opt., AO. 57 (2018) 365–369.
33 <https://doi.org/10.1364/AO.57.000365>.
34 [53] I.J. Bahl, Lumped Elements for RF and Microwave Circuits, Artech
35 House, Boston, 2003, pp. 171–172.

16 ↑ If possible equalize columns on the last page ↑